



Idealized Einstein-Podolsky-Rosen states from non-phase-matched parametric down-conversionC. Okoth ^{1,2}, E. Kovlakov ^{3,4}, F. Bönsel,^{1,2} A. Cavanna,^{1,2} S. Straupe,^{3,4} S. P. Kulik,^{3,4} and M. V. Chekhova^{1,2,3}¹Max Planck Institute for the Science of Light, Staudtstraße 2, 91058 Erlangen, Germany²University of Erlangen-Nürnberg, Staudtstraße 7/B2, 91058 Erlangen, Germany³Department of Physics, M. V. Lomonosov Moscow State University, Leninskie Gory, 119991 Moscow, Russia⁴Quantum Technologies Centre, M. V. Lomonosov Moscow State University, Leninskie Gory, 119991 Moscow, Russia

(Received 22 August 2019; revised manuscript received 3 December 2019; published 14 January 2020)

The most common source of entangled photons is spontaneous parametric down-conversion (SPDC). The degree of energy and momentum entanglement in SPDC is determined by the nonlinear interaction volume. By reducing the length of a highly nonlinear material, we relax the longitudinal phase-matching condition and reach record levels of transverse momentum entanglement. The degree of entanglement is estimated using both correlation measurements and stimulated emission tomography in wave-vector space. The high entanglement of the state in wave-vector space can be used to massively increase the quantum information capacity of photons, but more interestingly the equivalent state measured in position space is correlated over distances far less than the photon wavelength. This property promises to improve the resolution of many quantum imaging techniques beyond the current state of the art.

DOI: [10.1103/PhysRevA.101.011801](https://doi.org/10.1103/PhysRevA.101.011801)

Entanglement is a unique phenomenon that underpins many quantum technologies and applications, such as quantum imaging [1], quantum communication [2], and quantum computation [3]. Spontaneous parametric down-conversion (SPDC), the decay of a single high-energy photon into two lower-energy daughter photons, signal and idler, generates a state in which the two daughter photons are entangled. It has been used to successfully demonstrate effects such as the violation of Bell's inequalities and quantum teleportation [4,5]. Many of these famous experiments have been carried out by measuring the entangled state in a discrete-variable basis, for example, polarization. However, there has been a growing interest in continuous-variable (CV) entanglement, for example, in momentum, frequency, and quadrature amplitudes [6–8]. Measurements made in a CV basis provide access to a high-dimensional Hilbert space [9]. This, in turn, allows a large amount of information to be encoded in a relatively small number of photons, making CV entanglement desirable for quantum communication [10–12].

At a fixed frequency and fixed azimuthal angle the two-photon state generated via SPDC in (polar) angular space can be modeled [13] as

$$|\psi_{\theta_i, \theta_s}\rangle = C \int d\theta_i d\theta_s F(\theta_i, \theta_s) a_i^\dagger(\theta_i) a_s^\dagger(\theta_s) |0_s, 0_i\rangle, \quad (1)$$

where C is a normalization constant. The signal, $a_i^\dagger(\theta_i)$, and idler, $a_s^\dagger(\theta_s)$, creation operators generate photons into modes with wave vectors that subtend angles θ_i and θ_s with respect to the pump direction. The complex amplitude $F(\theta_i, \theta_s)$ dictates the degree of entanglement. In general, $F(\theta_i, \theta_s)$ can be separated into two factors, the pump and phase-matching functions, which depend on the transverse wave-vector mismatch, $\Delta k_\perp(\theta_i, \theta_s)$, and longitudinal wave-vector mismatch, $\Delta k_\parallel(\theta_i, \theta_s)$, respectively: $F(\theta_i, \theta_s) = F_p(\Delta k_\perp) F_{pm}(\Delta k_\parallel)$ (see Appendix). Their widths are determined by the inverse pump

beam waist σ and inverse length of the nonlinear material L . The joint probability density of the state, also known as the two-photon intensity (TPI), is given by $|F(\theta_i, \theta_s)|^2$. One can assign an unconditional or marginal distribution to the TPI which gives the single-photon angular emission width Δ_θ and a conditional distribution which gives the coincidence angular width δ_θ [14,15]. The ratio of the two widths is an operational measure of the degree of entanglement [16].

In the CV basis an idealized EPR state, $|\text{EPR}_{\theta_i, \theta_s}\rangle = \int d\theta_i d\theta_s \delta(\theta_i - \theta_s) a_i^\dagger(\theta_i) a_s^\dagger(\theta_s) |0_s, 0_i\rangle$, describes a maximally entangled state [17–19]. This corresponds to a situation where one photon out of the pair can be emitted into any angle, but once it has been detected, the emission angle of the conjugate photon in the pair is known to an infinite degree of accuracy. Therefore if $F(\theta_i, \theta_s) \rightarrow \delta(\theta_i - \theta_s)$, then the two-photon state is maximally entangled. For SPDC this ideal case can approximately be achieved when two conditions are fulfilled: (1) when L is decreased to the point that the phase-matching function becomes so broad that it can be approximated by 1 everywhere and (2) when σ is increased to the point that the pump function is so narrow that it can be approximated by a delta function with respect to the phase-matching function.

Recently, type-0 ($e \rightarrow ee$) two-photon radiation was observed from a microscale length of lithium niobate (LN) [20], which currently is the shortest L reported. At such length scales the phase-matching function $F_{pm}(\Delta k_\parallel)$ becomes massively broadened, leading to the generation of a highly entangled state. Until now SPDC has only been observed with the wave-vector mismatch zero or close to zero [21], such that momentum conservation was satisfied. However, for very small L this condition does not need to be upheld, allowing the transverse momentum to take any value, i.e., $\Delta k_\parallel(\theta_i, \theta_s) \neq 0$. This opens up the possibility of using materials with large second-order susceptibilities, that are normally disregarded in the phase-matched regime. In this way it is possible to

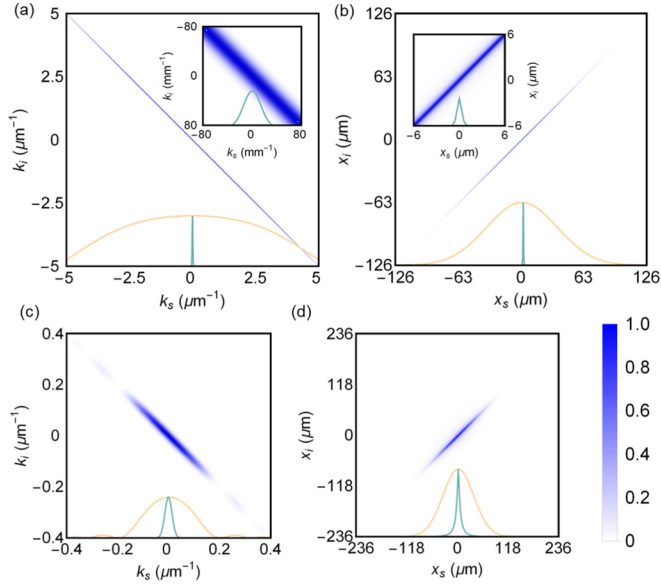


FIG. 1. Top: Theoretical TPI for non-phase-matched type-0 SPDC in LN in the (a) far field and (b) near field. The interaction length is $L = 1.38 \mu\text{m}$ and the pump beam is centered at 405 nm with a waist of $\sigma = 50 \mu\text{m}$. Bottom: TPI for phase-matched type-I collinear SPDC in LN in the (c) far field and (d) near field. The pump beam is centered on 532 nm with a waist of $\sigma = 50 \mu\text{m}$, however, the length is $L = 1.4 \text{ mm}$. The unconditional distributions are given by the light orange curves and the conditional distributions are given by the dark teal curves. The insets in (a) and (b) show a zoom of the TPI. Note the different scales between the phase-matched and non-phase-matched TPI.

partially compensate for the lower SPDC efficiency due to the reduced interaction length by using highly nonlinear materials. This leads to the surprisingly efficient generation of biphoton states via non-phase-matched SPDC. The TPI of a type-0 non-phase-matched biphoton state compared to a type-I phase-matched state, generated from a LN crystal pumped with the same beam waist, is shown in Fig. 1. In LN type-I phase matching can be satisfied using the birefringence of the material at wavelengths above 500 nm, however, below this value, due to the strong dispersion at shorter wavelengths, type-I phase matching cannot be satisfied. Although the conditional wave-vector width, governed only by the pump width, remains the same for both the phase-matched and non-phase-matched case, the unconditional wave-vector width for the non-phase-matched case is almost two orders of magnitude larger than in the phase-matched case. This difference can be increased further by reducing the crystal length to the nanoscale or subnanoscale.

The TPI in wave-vector (momentum) space corresponds to the emission as viewed in the far field. The corresponding TPI in the near-field or position space is given by the Fourier transform of the far-field TPI. For this reason, the coincidence width in the near field δ_x scales with the length L , while the single-photon positional width Δ_x is equal to the pump beam waist σ . If the length L is sufficiently small, then the correlation width in position can be deeply subwavelength while the uncertainty in the single-photon position is limited by the pump beam waist [see Fig. 1(b)].

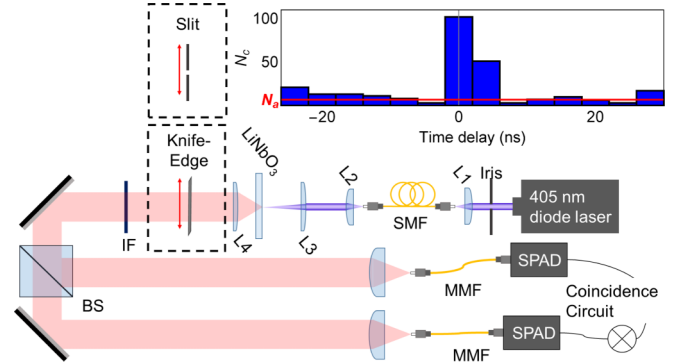


FIG. 2. Experimental setup for characterizing the TPI from spontaneously emitted photon pairs. The inset shows the number of coincidences N_c for different time delay bins. N_a is the number of accidental coincidences.

To investigate the TPI, both the full angular range Δ_θ of the photon pair emission and the angular correlation width δ_θ were measured. This was done using the setup shown in Fig. 2. The pump was a 30-mW continuous-wave laser centered at 405 nm. The pump was filtered spatially using a single-mode fiber (SMF) and focused (L3) into a layer of MgO-doped lithium niobate. The 3-in. LN wafer was fabricated with an inhomogeneous thickness. This meant that by moving the LN in the transverse plane it was possible to tune the interaction length L from 5.8 to 6.8 μm . However, the effective interaction length was limited not by the total length of the crystal but by the nonlinear coherence length [22], which at a pump wavelength of 405 nm is 1.38 μm . The X-cut LN was oriented such that the polarized pump interacted with the highest component ($\chi_{zzz}^{(2)}$) of the second-order susceptibility. L3 was selected to maximize the degree of entanglement, yet still allow the capture and detection of photon pairs. The chosen optimal focal length was 11 mm (see Appendix). Although this led to a relatively low degree of entanglement, the aim was to measure the large unconditional width, which is almost independent of the beam waist size. The resulting emission was collimated using a high numerical aperture (NA) aspheric lens with a 7.5 mm focal length (L4), to ensure that the full angular range of the emission was being collected, and filtered (IF) using an $810 \pm 5\text{-nm}$ bandpass filter.

To measure the total angular range of SPDC, the radiation was sent through a scanning knife edge. The radiation was then split into two arms using a beam splitter (BS), coupled into two multimode fibers (MMF) and sent to a Hanbury Brown–Twiss (HBT) setup, where the number of coincidence counts was recorded. The photons in each pair were anticorrelated in angle, which meant that scanning a knife edge across the angular range of the emission cut both the positive and negative angular ranges simultaneously. To ensure that we only registered SPDC correlations, the number of accidental coincidences was subtracted from the total number of coincidences. The number of accidental coincidences was found by measuring the total number of coincidences in a time window far from the arrival time difference of the signal and idler photons from LN (see the inset in Fig. 2). The ratio of the total number of coincidences N_c and the accidental coincidences N_a gives the value for the normalized

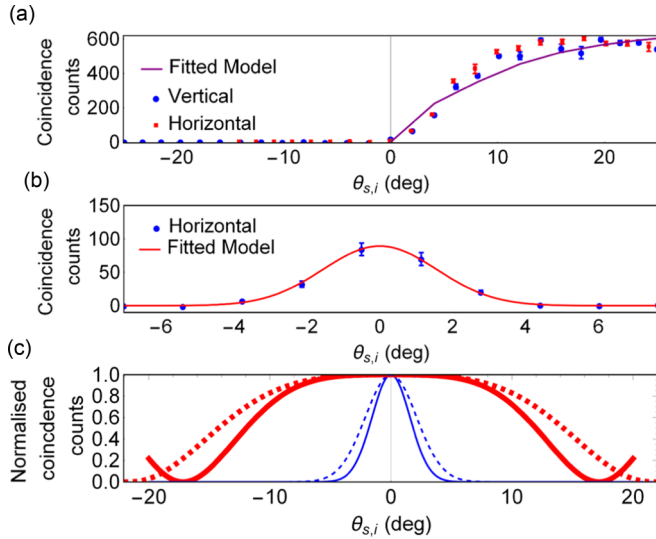


FIG. 3. Reconstruction of the unconditional and conditional angular distributions. (a) Number of coincidences acquired in 70 min for different positions of the knife edge (points) and their numerical fit (line). (b) Number of coincidences acquired in 30 min for different positions of the slit (points) and the expected Gaussian fit (line). The fitted models from (a) and (b) are plotted in (c), where the thick blue line is the unconditional width and the thin red is the conditional width, and compared to the theoretical distributions (dashed lines).

second-order correlation function $g^{(2)}$, which from the inset in Fig. 2 is roughly 10. Type-0 SPDC emission is azimuthally symmetric, therefore the number of coincidence counts should be given by the angular spectrum of SPDC, integrated from the knife edge position to the position of collinear emission ($\theta_{i,s} = 0^\circ$). Figure 3(a) shows the number of coincidences at different knife edge positions (points), with a numerical fit of the expected distribution [13] (line). Blue circles and red squares correspond to scanning in the vertical and horizontal directions, respectively. Their overlap confirms the azimuthal symmetry of the experiment.

To measure the conditional width of the TPI, the scanning knife edge was replaced by a slit in front of the collimated emission. Again the emission was split and sent to a HBT setup and the number of coincidences was measured. The slit was scanned across the collinear direction of the radiation. The results, shown as the points in Fig. 3(b), are fitted with a Gaussian (solid line). The fitted conditional and unconditional angular distributions are then compared in Fig. 3(c) (thin and thick solid lines, respectively) with the corresponding theoretical distributions (thin and thick dashed lines, respectively). Just taking the central peak of the unconditional angular width into account gives a full width at half maximum (FWHM) of roughly 25° which, at a fixed frequency, is many times larger than for a conventional phase-matched SPDC source.

To measure the TPI in the case of softly focused pump, leading to a high degree of entanglement, stimulated emission tomography (SET) [23] was implemented. A seed beam stimulated the emission of the idler photon, which led to enhanced emission in the signal mode. While SET is typically implemented in the frequency domain, here we have used it to probe the TPI in angular space. In angular SET, as opposed to frequency-based SET, the frequencies of the signal and

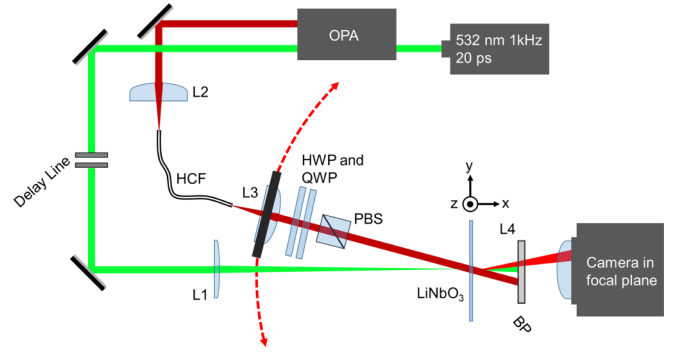


FIG. 4. The setup for angular SET. Lens L3 is placed on a rotation platform along with the half-wave plate (HWP), quarter-wave plate (QWP), and polarizing beam splitter (PBS). BP is a bandpass filter centered at 800 nm with a bandwidth of 10 nm. HCF is a hollow-core fiber. Lenses L3 and L2 are used to couple in and out of the HCF, while lens L1 is interchangeable to control the beam waist.

idler modes need to be fixed, instead of the spatial modes. We fix the frequency mode by making the seed, generated from the output of the optical parametric amplifier (OPA), narrowband (<1 nm FWHM spectral bandwidth). Typically, in a nonseeded SPDC measurement, the momentum entanglement is measured by fixing the signal and idler frequencies using a bandpass filter (≈ 10 nm) [18,19]. Compared to a bandpass filter, the angular SET measurement fixes the frequencies with a far higher accuracy. This, however, does not matter due to the ultrabroad spectral width of non-phase-matched SPDC [20].

SET allowed us to measure the signal emission directly using a SPIRICON camera (Fig. 4), without resorting to single-photon detectors. To reconstruct the full angular TPI, we stimulated the idler at all possible emission directions. This was done by changing the incident angle of the seed beam impinging on the LN sample. The second harmonic of a Nd:YAG laser at 532 nm, with a 20 ps pulse width and 1 kHz repetition rate, was used as the pump. The seed was centered at 1600 nm with the same pulse properties as the pump and a pulse energy of $10 \mu\text{J}$. It was coupled into a high damage threshold hollow-core fiber (HCF). The outcoupler was placed on a rotation platform and the seed beam was sent through a half-wave plate (HWP), quarter-wave plate (QWP), and polarizer (PBS) to ensure the seed was polarized along the z axis of the LN crystal. A delay line ensured that the pump and seed pulses arrived simultaneously at the LN. Lens L1 was used to focus the pump and to check how the degree of entanglement changed with the beam size. The LN was placed at the focal point of the pump, coinciding with the center of rotation of the platform. The seed was unfocused on the sample, so that it could be approximately described by a plane wave, compared to the pump beam. To reconstruct the TPI, the incidence angle of the seed was scanned and the intensity distribution of the signal (797-nm) beam was recorded on a camera in the Fourier plane (Fig. 5). To filter out the pump and seed beam, a bandpass filter (BP), centered at 800 ± 5 nm, was placed before the camera. To calibrate the emission angles of the signal beam, the second-harmonic generation (800 nm) of the seed beam was used.

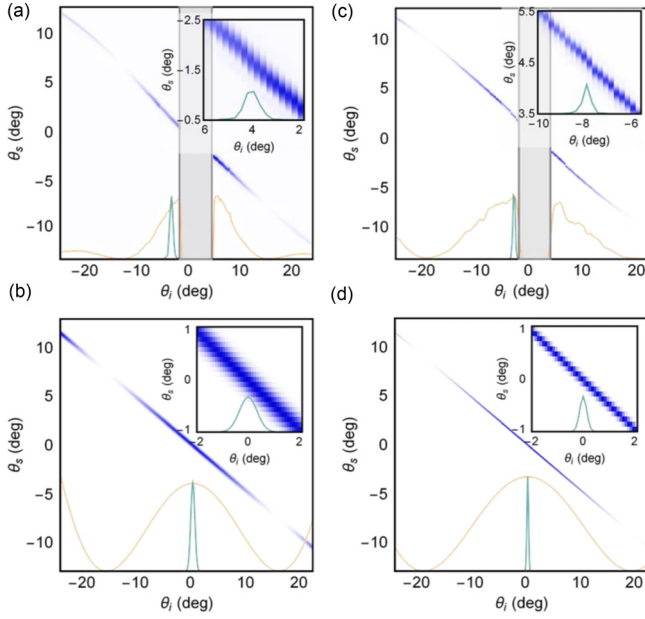


FIG. 5. Angular TPI for non-phase-matched SPDC measured via SET. Top panels: The TPI measured for (a) pump beam waist of $\sigma = 60 \mu\text{m}$ and interaction length $L = 6.7 \mu\text{m}$ and (c) pump beam waist of $\sigma = 120 \mu\text{m}$ and interaction length $L = 6.4 \mu\text{m}$. Bottom panels (b) and (d) show the calculated TPI for the corresponding cases, respectively. The insets show a zoom of the TPI to see the scale of the conditional curve (dark teal).

The TPI was measured at two positions on the LN wafer, corresponding to $L = 6.3 \mu\text{m}$ and $L = 6.6 \mu\text{m}$, and using two different lenses (L1), with focal lengths 200 and 100 mm, respectively. Figures 5(a) and 5(c) demonstrate the TPI measured for these two sets of parameters. The data between roughly -3° and 3° are missing because the optics behind the seed beam blocked the pump. The small discrepancy between the theory [Figs. 5(b) and 5(d)] and experiment can be attributed to both lens aberrations and reflection losses at large incident and collection angles.

The ratio between the emission (unconditional) width $\Delta = 19.5^\circ$ and the correlation (conditional) width $\delta = 0.5^\circ$, from Fig. 5(c), gives $R_{1D} = 39$. This is in good agreement with the theoretical value of $R_{1D} = 37$. Accounting for both transverse coordinates, the total Fedorov ratio across a cross section of the beam is roughly $R_{2D} = 1200$. The Schmidt number for the theoretical TPI in Fig. 5(d) gives $K = 39$, which agrees well with the Fedorov ratio. Note that both these numbers underestimate the degree of entanglement as they do not take into account the high side lobes of the TPI [24]. For practical applications, collection of such a broad angular distribution is difficult. However, high NA multimode fibers (NA = 0.5) with a large core diameters ($\approx 200 \mu\text{m}$) are more than suitable to collect SPDC emission from microscale layers [25,26].

In conclusion, we have shown that photon pairs generated in an ultrathin layer of lithium niobate via non-phase-matched SPDC can be emitted into a broad range of angles with respect to the pump propagation at a fixed frequency. The large angular width, combined with a narrow correlation width, means that the state displays huge transverse entanglement.

Here, we have estimated and inferred the degree of entanglement using two indirect methods. For a full characterization of the entanglement the near-field correlations should also be investigated. This is technically challenging due to the subwavelength nature of the correlation width in position. The state generated in such a process is not dissimilar to the state imagined by Einstein, Podolsky, and Rosen in 1935, and by moving to even thinner platforms on which to generate photon pairs it may be possible to closely imitate the system they proposed. Although the rate of two-photon emission from non-phase-matched SPDC is low, there is still scope to optimize this. For example, semiconductors promise far higher second-order susceptibilities, which could dramatically improve the emission rate [22,27]. In addition, structuring materials may lead to a Purcell enhancement [28]. With higher two-photon emission rates, and the high degree of entanglement reported here, non-phase-matched SPDC could surpass any source reported so far.

Not only does the large degree of entanglement mean a large quantum information capacity, it can also improve the resolution of imaging with quantum light. Several quantum imaging techniques have been proposed and implemented over the years, most of them based on entangled photons [29–31]. The spatial resolution of these techniques, as with all imaging techniques, is limited by the range of transverse wave vectors emitted. Due to the large number of transverse wave-vector modes generated from non-phase-matched thin layers, using SPDC generated from a thin layer should improve the resolution limits of quantum imaging techniques.

Here, we have only investigated the far-field correlation distribution experimentally, and an interesting step would be to investigate the near-field correlations [Fig. 1(b)]. In the near field the crystal length determines the correlation width in position. If the crystal length is sufficiently small, then the correlation width will be subwavelength. Fundamentally, the interaction length is limited by an atomically thick monolayer, such as molybdenum disulfide [32]. Using a monolayer would increase the correlation resolution in position to the deeply subwavelength regime. Implementing non-phase-matched SPDC as a pump in a two-photon microscopy setup and relying on the excitation of a fluorescent (or absorbent) material by correlated photons would allow imaging well beyond the Abbe diffraction limit.

We acknowledge the financial support by Deutsche Forschungsgemeinschaft (DFG) (CH-1591/3-1).

APPENDIX

1. Knife edge reconstruction

For an interaction length limited by the nonlinear material boundaries and interaction area limited by the pump beam waist, the form of the pump and phase-matching functions is

$$F_p(\Delta k_\perp) = \exp\left(-\frac{\Delta k_\perp^2 \sigma^2}{2}\right), \quad (\text{A1})$$

$$F_{pm}(\Delta k_\parallel) = \text{sinc}\left(\frac{\Delta k_\parallel L}{2}\right)^2, \quad (\text{A2})$$

where the pump beam waist σ is the width of one standard deviation. The fit for the slit measurement was simply given by F_p . As this is a Gaussian function there is no difference in width between a one-dimensional (1D) distribution and a 2D symmetric distribution. To fit the knife edge measurement the integrated value of F_{pm} was taken in two dimensions, $\Delta k_{\parallel} = \sqrt{\Delta k_x^2 + \Delta k_y^2}$. To account for the scanning knife edge and because we were collecting coincidences, the integration boundaries over k_x were reduced symmetrically. The argument $\Delta k_{\parallel}(\theta_i, \theta_s)$ was used as the fitting parameter and the integrated sinc function was fitted by hand to match the curve in Fig. 3(b).

2. Collection efficiency in the spontaneous regime

Non-phase-matched SPDC is not only inefficient but also difficult to collect due to the highly multimode nature of the emission. Although we were working with multimode detectors, spherical aberrations and differing mode divergences led to a restricted number of modes able to be detected efficiently. Reducing the number of modes by reducing the pump beam waist led to an increase in detection efficiency at the expense

of low entanglement. This is the reason for choosing a high NA lens for L3 in the correlation experiment. Increasing the efficiency of the non-phase-matched source would be one way to increase the detection probability of a highly entangled state. Similarly, improving detection losses in the setup would allow us to detect a more highly entangled state. The quantum efficiency of the multimode detectors was around 50%, leading to a correlation efficiency of 25%. The bandpass filter (IF) used had a transmission of 50% and bandwidth of 10 nm. Internal reflection caused by the high refractive index of the LN dropped the efficiency by an additional 20%. These values could be improved to yield higher correlation rates, for example, by optimizing the bandpass filter, using antireflection coating at the correct frequency, and using superconducting nanowires as opposed to avalanche diodes. Lastly, the huge angle of emission of non-phase-matched SPDC requires a large NA lens to capture it. For the correlation measurement the lens (L4) had an NA = 0.3. This coincided almost with the emission angle of the radiation expected theoretically. Without knowing the crystal length precisely at a given point on the LN wafer, it was difficult to discern whether the lens aperture limited the emission angle.

-
- [1] M. I. Kolobov, *Quantum Imaging* (Springer, Berlin, 2007).
- [2] N. Gisin and R. Thew, Quantum communication, *Nat. Photonics* **1**, 165 (2007).
- [3] M. A. Nielsen and I. L. Chuang, *Quantum Computation and Quantum Information* (Cambridge University Press, Cambridge, UK, 2000).
- [4] D. Boschi, S. Branca, F. De Martini, L. Hardy, and S. Popescu, Experimental Realization of Teleporting an Unknown Pure Quantum State Via Dual Classical and Einstein-Podolsky-Rosen Channels, *Phys. Rev. Lett.* **80**, 1121 (1998).
- [5] Y. H. Shih and C. O. Alley, New Type of Einstein-Podolsky-Rosen-Bohm Experiment using Pairs of Light Quanta Produced by Optical Parametric Down Conversion, *Phys. Rev. Lett.* **61**, 2921 (1988).
- [6] S. L. Braunstein and P. van Loock, Quantum information with continuous variables, *Rev. Mod. Phys.* **77**, 513 (2005).
- [7] C. K. Law and J. H. Eberly, Analysis and Interpretation of High Transverse Entanglement in Optical Parametric Down Conversion, *Phys. Rev. Lett.* **92**, 127903 (2004).
- [8] C. K. Law, I. A. Walmsley, and J. H. Eberly, Continuous Frequency Entanglement: Effective Finite Hilbert Space and Entropy Control, *Phys. Rev. Lett.* **84**, 5304 (2000).
- [9] E. Bolduc, G. Gariépy, and J. Leach, Direct measurement of large-scale quantum states via expectation values of non-Hermitian matrices, *Nat. Commun.* **7**, 10439 (2016).
- [10] Y. Adachi, T. Yamamoto, M. Koashi, and N. Imoto, Simple and Efficient Quantum Key Distribution with Parametric Down-Conversion, *Phys. Rev. Lett.* **99**, 180503 (2007).
- [11] T. Jennewein, C. Simon, G. Weihs, H. Weinfurter, and A. Zeilinger, Quantum Cryptography with Entangled Photons, *Phys. Rev. Lett.* **84**, 4729 (2000).
- [12] A. Mair, A. Vaziri, G. Weihs, and A. Zeilinger, Entanglement of the orbital angular momentum states of photons, *Nature (London)* **412**, 313 (2001).
- [13] C. H. Monken, P. H. Souto Ribeiro, and S. Pádua, Transfer of angular spectrum and image formation in spontaneous parametric down-conversion, *Phys. Rev. A* **57**, 3123 (1998).
- [14] M. V. Fedorov, M. A. Efremov, P. A. Volkov, E. V. Moreva, S. S. Straupe, and S. P. Kulik, Spontaneous parametric down-conversion: Anisotropic and anomalously strong narrowing of biphoton momentum correlation distributions, *Phys. Rev. A* **77**, 032336 (2008).
- [15] M. V. Fedorov, M. A. Efremov, P. A. Volkov, E. V. Moreva, S. S. Straupe, and S. P. Kulik, Anisotropically and High Entanglement of Biphoton States Generated in Spontaneous Parametric Down-Conversion, *Phys. Rev. Lett.* **99**, 063901 (2007).
- [16] M. V. Fedorov, M. A. Efremov, A. E. Kazakov, K. W. Chan, C. K. Law, and J. H. Eberly, Packet narrowing and quantum entanglement in photoionization and photodissociation, *Phys. Rev. A* **69**, 052117 (2004).
- [17] A. Einstein, B. Podolsky, and N. Rosen, Can quantum-mechanical description of physical reality be considered complete? *Phys. Rev.* **47**, 777 (1935).
- [18] J. C. Howell, R. S. Bennink, S. J. Bentley, and R. W. Boyd, Realization of the Einstein-Podolsky-Rosen Paradox Using Momentum- and Position-Entangled Photons from Spontaneous Parametric Down Conversion, *Phys. Rev. Lett.* **92**, 210403 (2004).
- [19] M. P. Edgar, D. S. Tasca, F. Izdebski, R. E. Warburton, J. Leach, M. Agnew, G. S. Buller, R. W. Boyd, and M. J. Padgett, Imaging high-dimensional spatial entanglement with a camera, *Nat. Commun.* **3**, 984 (2012).
- [20] C. Okoth, A. Cavanna, T. Santiago-Cruz, and M. V. Chekhova, Microscale Generation of Entangled Photons Without Momentum Conservation, *Phys. Rev. Lett.* **123**, 263602 (2019).
- [21] H. Di Lorenzo Pires, C. H. Monken, and M. P. van Exter, Direct measurement of transverse-mode entanglement in two-photon states, *Phys. Rev. A* **80**, 022307 (2009).

- [22] R. W. Boyd, *Nonlinear Optics* (Elsevier, Amsterdam, 2003).
- [23] M. Liscidini and J. E. Sipe, Stimulated Emission Tomography, *Phys. Rev. Lett.* **111**, 193602 (2013).
- [24] M. Reichert, X. Sun, and J. W. Fleischer, Quality of spatial entanglement propagation, *Phys. Rev. A* **95**, 063836 (2017).
- [25] D. Richardson, J. Fini, and L. E. Nelson, Space-division multiplexing in optical fibres, *Nat. Photonics* **7**, 354 (2013).
- [26] L. V. Amitonova, T. B. H. Tentrup, I. M. Vellekoop, and P. W. H. Pinkse, Multimode-fiber-based high-dimensional quantum secure communication, [arXiv:1801.07180](https://arxiv.org/abs/1801.07180).
- [27] S. Liu, M. B. Sinclair, S. Saravi, G. A. Keeler, Y. Yang, J. Reno, G. M. Peake, F. Setzpfandt, I. Staude, T. Pertsch *et al.*, Resonantly enhanced second-harmonic generation using III-V semiconductor all-dielectric metasurfaces, *Nano Lett.* **16**, 5426 (2016).
- [28] A. Davoyan and H. Atwater, Quantum nonlinear light emission in metamaterials: Broadband Purcell enhancement of parametric downconversion, *Optica* **5**, 608 (2018).
- [29] G. Brida, M. Genovese, and I. R. Berchera, Experimental realization of sub-shot-noise quantum imaging, *Nat. Photonics* **4**, 227 (2010).
- [30] G. B. Lemos, V. Borish, G. D. Cole, S. Ramelow, R. Lapkiewicz, and A. Zeilinger, Quantum imaging with undetected photons, *Nature (London)* **512**, 409 (2014).
- [31] T. B. Pittman, Y. H. Shih, D. V. Strekalov, and A. V. Sergienko, Optical imaging by means of two-photon quantum entanglement, *Phys. Rev. A* **52**, R3429 (1995).
- [32] H. D. Saleh, S. Vezzoli, L. Caspani, A. Branny, S. Kumar, B. D. Gerardot, and D. Faccio, Towards spontaneous parametric down conversion from monolayer MoS₂, *Sci. Rep.* **8**, 3862 (2018).